Supporting material for: Allometric cell spreading and the geometrical control of focal adhesion collective organization

Célian Bimbard[1,†], Ali-Alhadi Wahhod[2,†], Démosthène Mitrossilis[3], Joseph Vermeil[1], Rémi Bousquet[4,5], Alain Richert[1], David Pereira[1], Pauline Durand-Smet[1], Sophie Asnacios[1], Jocelyn Étienne[2], Atef Asnacios[1], and Jonathan Fouchard[4,5]

[1]Université Paris Cité, CNRS UMR 7057, Laboratoire Matière et Systèmes Complexes, Paris, France; [2]Université Grenoble Alpes, CNRS UMR 5588, Laboratoire Interdisciplinaire de Physique, Grenoble, France; [3]Biomedical Research Foundation of the Academy of Athens, Athens, Greece; [4]Sorbonne Université, CNRS UMR 8263, INSERM U1345, Development, Adaptation and Ageing, Paris, France; [5]Sorbonne Université, Institut de Biologie Paris Seine (IBPS), Paris, France; [†]These authors contributed equally to this work.

Appendix 1 : Geometrical description of cell spreading

1. Model

The simplest model of cell body shape corresponds to assume that it is governed only by cortical actomyosin tension and plasma membrane-regulated volume. This has been shown to lead to consistent predictions during cell spreading on two plates (1). Volume regulation implies a pressure difference across the membrane (and the thin actomyosin cortex apposed to it), this pressure equilibrates spatially at a timescale much shorter than spreading (2). Following (3) we further assume that the cortex is under a uniform isotropic tension $\sigma(t)$ and axial symmetry of the shape. The shape of the cell cortex in those conditions can be parameterised as $\Gamma = \{r(z,t), z_{\min} \leq z \leq z_{\max}\}$ and the volume of the cell body can be calculated by:

$$V(t) = \pi \int_{z_{\min}}^{z_{\max}} r(z,t)^2 \mathrm{d}z$$

It obeys the Young-Laplace equation:

$$H(t) = \frac{r''}{\left(1+r'^2\right)^{3/2}} - \frac{1}{r\sqrt{1+r'^2}} = \frac{\Delta p}{\sigma} \qquad [1]$$

where $r' = \mathrm{d}r/z$, $\Delta p(t)$ is the pressure difference between the interior and exterior and we define H the mean curvature. Given uniform pressure and tension, H is uniform in space and thus the shape has constant mean curvature and can be a portion of sphere, cylinder, unduloid or nodoid (Fig. S5-C).

For single plate spreading, the only appropriate shape is obviously a spherical cap and it can be readily shown that for a given volume V and basal radius R_b there is only one solution to Eq 1. The ratio $\frac{\Delta p}{\sigma}$ of pressure difference and tension is thus deduced from the volume.

For the spreading between two plates, the shape can be either of a nodoid, unduloid or cylinder depending on the respective values of R_b and V. Similar to the single plate case, being given these two values, a unique shape and the corresponding ratio $\frac{\Delta p}{\sigma}$ of pressure difference and tension can be deduced.

In what follows, we reproduce the sequence of shapes of a cell during spreading, either in unconfined (single plate) or confined (parallel plates) geometry, by assuming that it maintains a constant volume $V = V_0$ and varying its radius $R_b(t)$.

2. Single plate geometry: spherical cap

Given $R_b(t)$ and V_0, it can be easily verified that spheres of parametric equation

$$\begin{cases} z(s) = R_{cap}(1-\cos(s)) + z_0 \\ r(s) = R_{cap}\sin(s) \end{cases}$$

for a curvilinear coordinate $s \in [0, s_f]$, with $z_0(t) = \pm\sqrt{R_{cap} - R_b}$ and $s_f = \arccos\left(\frac{R_{cap}+z_0}{R_{cap}}\right)$ are solutions. We calculate the radius of curvature $R_{cap}(t) = 2/H(t)$ such that the spherical cap volume $V(t) = \frac{\pi}{6}(R_{cap}+z_0)(3R_b^2 + (R_{cap}+z_0)^2)$ is equal to V_0.

The (outer) contact angle at the plate can be calculated as $\cot\theta = -\frac{\mathrm{d}r}{\mathrm{d}z}$, resulting in $\theta = \cos^{-1}(z_0/R_{cap})$.

3. Two plates geometry

When spreading between two parallel plates spaced by height h, we assume that the shape is symmetric with respect to the plane $z = 0$ parallel to the plates $z = \pm h/2$ and at equal distance from them. Thus the surface forms a right angle with this plane, $r'(z=0) = 0$. The additional conditions are that $r(z = h/2) = R_b(t)$ and, as above, volume $V(t) = V_0$ allows to set $H(t)$. We proceed with an additional intermediate unknown, $r(z = 0, t) = R_e(t)$: for a given t, we initialise $R_e(t)$ to a first guess $R_e^0(t)$ and use a fixed point algorithm on R_e^i to reach $V(t) = V_0$.

The problem of integration of nonlinear Eq 1 is thus done with boundary conditions:

$$\begin{cases} r(s_i,t) = R_e(t), & z(s_i) = 0 \\ r(s_f) = R_b(t), & z(s_f) = h/2 \\ \frac{\mathrm{d}r}{\mathrm{d}z}(s_i) = 0 \end{cases} \qquad [2]$$

It is known (4) that depending on R_e, the solution can belong to five families of curves: nodoids for $R_e^2 < R_b^2 + (h/2)^2$, a sphere when $R_e^2 = R_b^2 + (h/2)^2$, an unduloid for intermediate values of R_e (but a cylinder for $R_e = R_b$), a catenoid when $R_e = R_e^*$ such that $R_e^* \cosh(h/(2R_e^*)) = R_b$ and nodoids again when $R_e > R_e^*$. In practice, for the range of $R_b(t)$ that is useful to compare with experiments, we find that $R_e < R_e^*$. Note that spheres, cylinders and catenoids can be seen as limiting cases of unduloids or nodoids.

A. Unduloid. Its parametric representation (5) is:

$$\begin{cases} z(s) = \dfrac{b^2}{a}\displaystyle\int_0^s I_u(u)\mathrm{d}u + z_0, \\ r(s) = b\sqrt{\dfrac{1-\xi_u\cos s}{1+\xi_u\cos s}}. \end{cases} \quad [3]$$

where

$$I_u(u) = \frac{1}{(1+\xi_u\cos u)\sqrt{1-\xi_u^2\cos^2 u}},$$

and s is a curvilinear coordinate varying in a range $[s_i, s_f]$ which is to be determined, whereas a, b and $\xi_u = \sqrt{1-\dfrac{b^2}{a^2}}$ are positive parameters also to be determined. It can be shown that such curves obey the equation:

$$1+\left(\frac{dr}{dz}\right)^2 = \frac{4a^2r^2}{\left(r^2+b^2\right)^2} \quad [4]$$

which in turn verify Eq 1 with $H = \pm 1/(2a)$.
Because $r(s_i) = R_e$ is the minimum of r if $R_e < R_b$ (resp. the maximum else), $s_i = 0$ (resp. $s_i = \pi$). Rewriting $b = a\sqrt{1-\xi_u^2}$ and using the boundary condition $r(s_f) = R_b$, the parameters b, s_i and s_f can be expressed as functions of ξ_u and a. The additional boundary condition $r'(z=0) = 0$ injected in Eq 4, yields two possible values of a as a function of ξ_u,

$$a(\xi_u) = \frac{R_e(1-\chi\xi_u)}{1-\xi_u^2}$$

where $\chi = \pm 1$. It can be shown that χ has to have the same sign as $R_e - b$ (6), which has the same as the sign as $R_e - R_b$. The remaining parameter, ξ_u, can be determined from the implicit equation

$$h/2 = z(s_f(\xi_u, R_b)) = \frac{b(\xi_u)^2}{a(\xi_u)}\int_{s_i}^{s_f(\xi_u,R_b)} I_u(\xi_u, s)\mathrm{d}s \quad [5]$$

As above, the angle at the bottom plate can be found using $\cot\theta = -\dfrac{\mathrm{d}r}{\mathrm{d}z}(-s_f)$.

B. Nodoid. Its parametric representation (5) is:

$$\begin{cases} z(s) = \dfrac{b^2}{a}\displaystyle\int_0^s I_n(u)\,\mathrm{d}u + z_0, \\ r(s) = b\sqrt{\dfrac{\xi_n-\cos s}{\xi_n+\cos s}}. \end{cases} \quad [6]$$

where

$$I_n(u) = \frac{\cos u}{(\xi_n+\cos u)\sqrt{\xi_n^2-\cos^2 u}},$$

and $s \in [s_i, s_f]$, a range to be determined. The positive parameters a, b, and $\xi_n = \sqrt{1+\dfrac{b^2}{a^2}}$ obey the governing differential equation:

$$1+\left(\frac{\mathrm{d}r}{\mathrm{d}z}\right)^2 = \frac{4a^2r^2}{\left(r^2-b^2\right)^2}. \quad [7]$$

Similarly to the unduloid case, and using the boundary condition at $z = 0$, a can again be expressed as a function of ξ_n:

$$a(\xi_n) = \frac{R_e(\chi-\xi_n)}{1-\xi_n^2}.$$

The remaining parameter, ξ_n, is determined by solving the implicit equation:

$$h/2 = z(s_f(\xi_n, R_b)) = \frac{b(\xi_n)^2}{a(\xi_n)}\int_{s_i}^{s_f(\xi_n,R_b)} I_n(\xi_n, s)\,\mathrm{d}s, \quad [8]$$

where the integration bounds s_i and s_f are defined based on the boundary conditions.

C. Implementation and upper limit. In Figure 5, we set $V_0 = \frac{4}{3}\pi R_0^3$, where $R_0 = 8.83\mu$m for untreated cells, and $h = 1.9R_0$, in accordance with the experimental conditions. For R_b varying over the range of experimentally observed values, we then calculate the shape of spherical caps of volume V_0, and of either unduloids or nodoids of volume V_0 and height h, as detailed above. We can then deduce the angle that these shape make with the substrate.
There is a lower bound for the volume enclosed in a CMC surface of rotational symmetry having radius $r = R_b$ at $z = h/2$, however to the best of our knowledge there is no general formula allowing to compute it. In practice, we find that solutions cease to exist for our choice of parameters V_0 and h beyond a radius $R_b^* \simeq 13\mu$m. There does not exist, e.g., a section of catenoid of height h that has volume V_0. The physical understanding of this geometrical limitation is that the model must cease to be valid for cells observed with $R_b > R_b^*$: it is e.g. possible that the symmetries assumed here (axial symmetry, isotropy of the tension) cease to be a fair approximation.

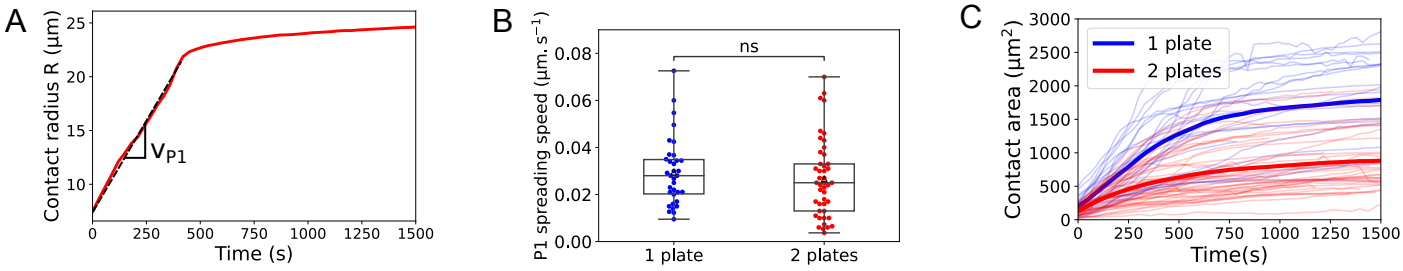

Fig.S 1. A - Cell-substrate contact radius as a function of time of a typical Ref-52 fibroblast spreading on a bi-dimensional substrate. v_{P1} describes the spreading speed during the first phase of spreading. B - Boxplot representing the spreading speed during the first phase of spreading P1 in the single plate and parallel plates geometry. C - Contact area as a function of time for all samples tested in the single plate (blue) and parallel plates (red) geometry. Bold lines represent the mean value calculated over all samples at each time-point.

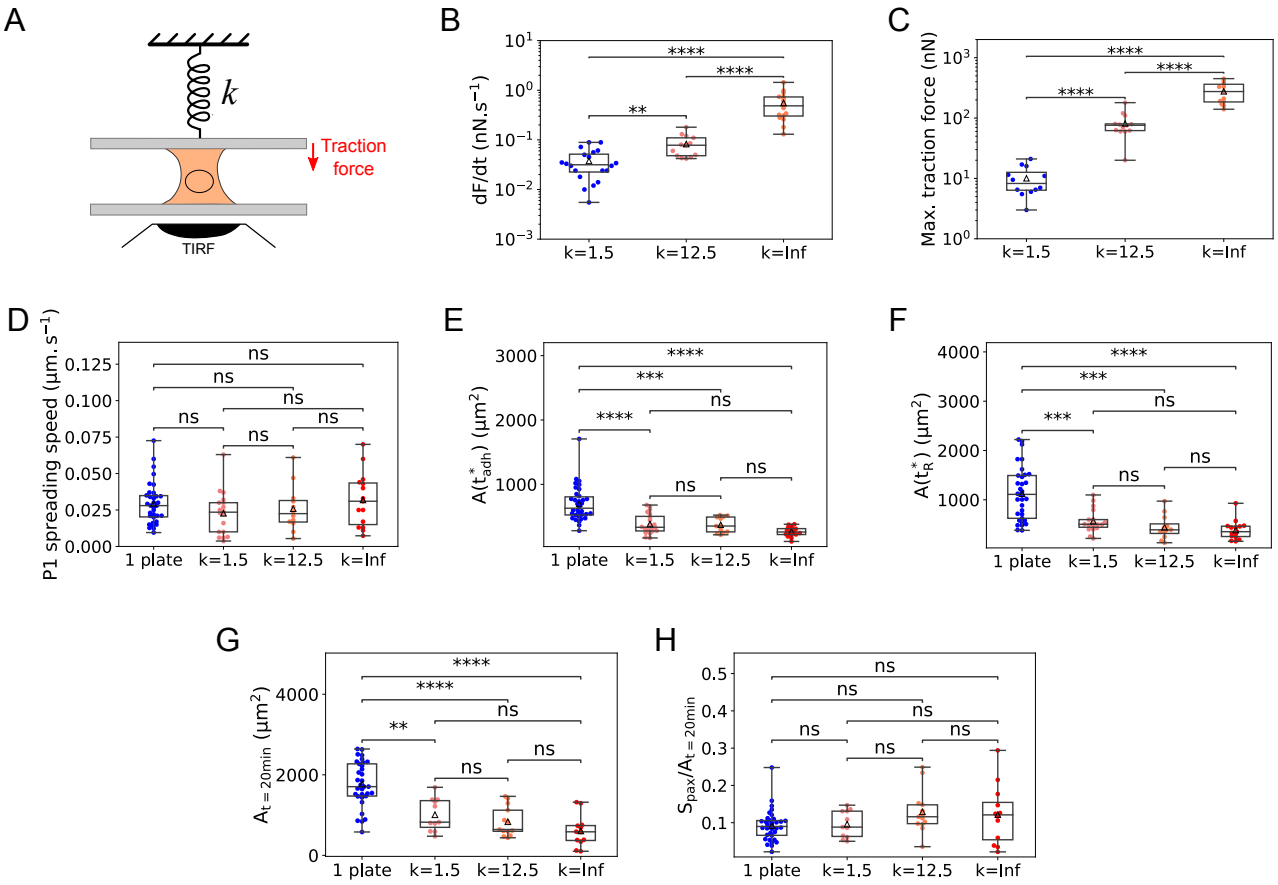

Fig.S 2. Effect of upper plate stiffness on cell traction, spreading and focal adhesions formation (k=1.5 nN/µm, N=17; k=12.5 nN/µm, N=11 and infinite stiffness, N=14) and comparison with single plate experiment ('1 plate'). A - Sketch of parallel plate setup. The upper plate is flexible, with stiffness k. TIRF imaging is performed at the bottom, rigid plate. B - Maximum rate of traction force increase. C - Maximum traction force. D - Spreading rate during the first phase of spreading (P1). E - Contact area $A(t^*_{adh})$ at which paxillin starts forming aggregates. F - Contact area $A(t^*_R)$ at transition between spreading phases. G- Cell-substrate contact area after 20 minutes of spreading. H - Ratio of focal adhesions ring area over cell-substrate contact area after 20 minutes of spreading.

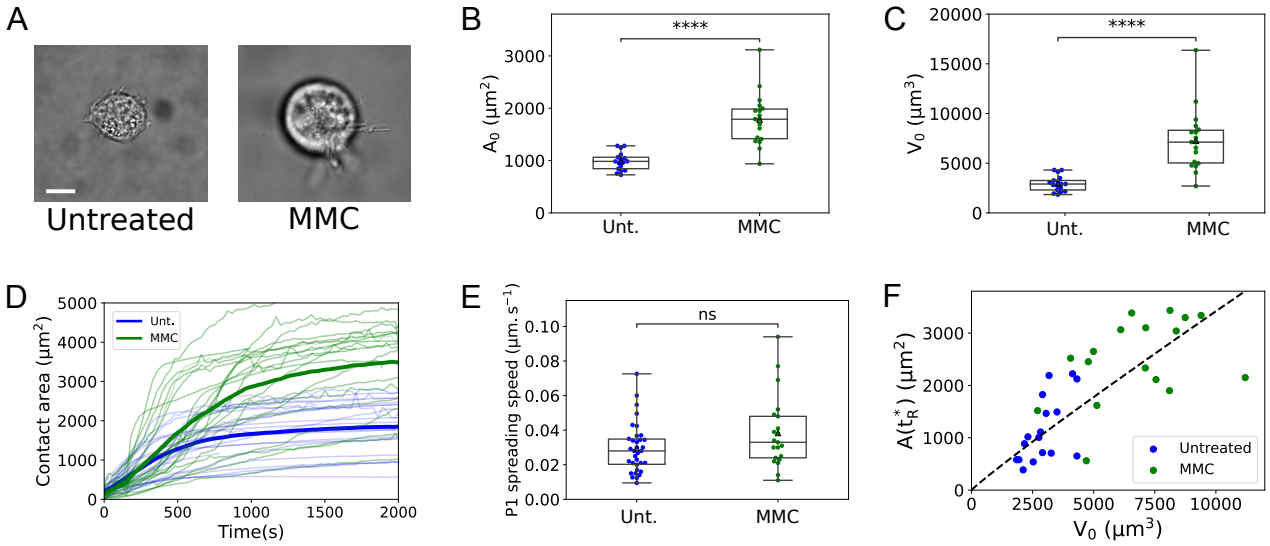

Fig.S 3. Effect of mitomycin C treatment (0.25µM, 2 days) on cell size in suspension. A - Bright-field images of Ref-52 fibroblast in suspension treated (MMC, right) or not (Untreated, left) with mitomycin C. Scale bar: 10µm. B - Effect of mitomycin C treatment on cell surface in suspension. C - Effect of mitomycin C treatment on cell volume in suspension. D - Contact area as a function of time for all untreated (Unt., blue) and mitomycin C treated (MMC, green) samples. Bold lines represent the mean value calculated over all samples at each time-point. E - Boxplot representing the spreading speed during the first phase of spreading P1 for untreated and mitomycin C-treated samples. F - Contact area $A(t_R^*)$ as a function of cell volume in suspension V_0 in untreated (blue) and Mitomycin C treated cells (green). Dotted line: power-law fit of exponent 0.94, close to 1.

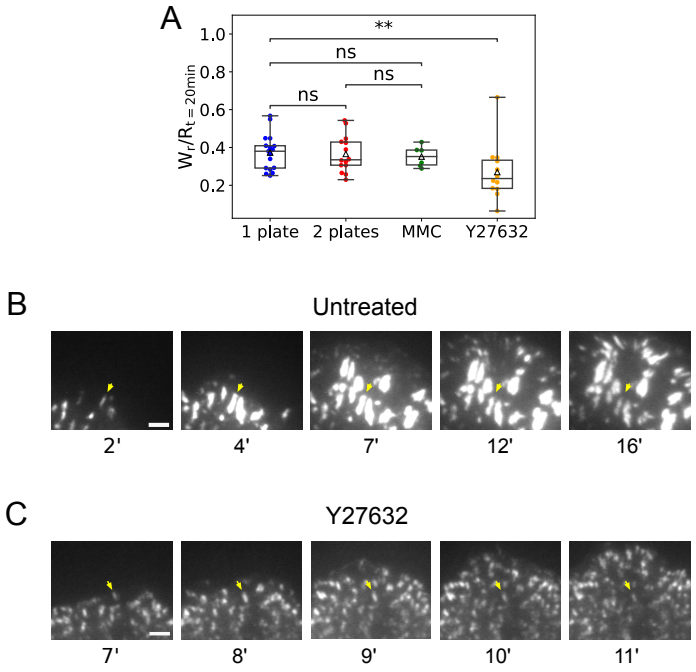

Fig.S 4. A - Width of the focal adhesions ring versus contact radius along the second phase of spreading P2 for the single plate (blue), parallel plates (red) and MMC treated cells spreading on a single plate (green). B - Typical event of paxillin aggregate formation and turnover during spreading of an untreated cell. Yellow arrow points to the cluster of interest. C - Same as in A for a cell treated with ROCK inhibitor (Y27632). Scale bars: 2µm.

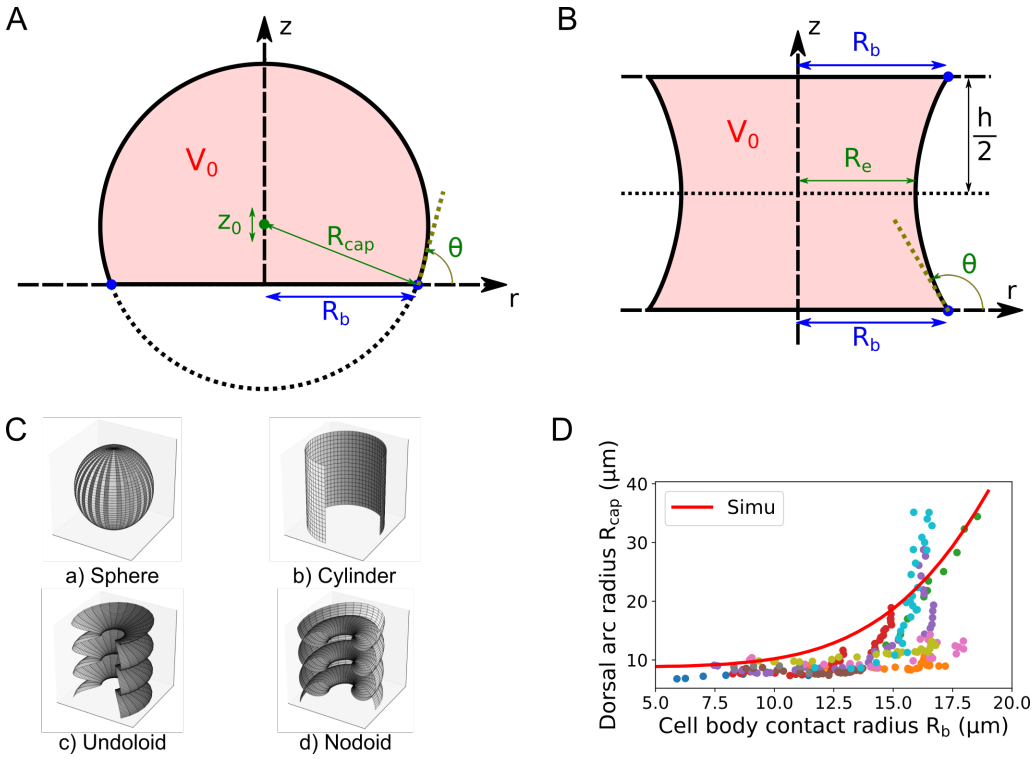

Fig.S 5. Geometrical description of cell spreading. A - Cell shape on a single plate is modeled as a spherical cap of main radius R_{cap} and center $(0, z_0)$. These parameters are calculated so that the spherical cap volume is equal to V_0 and that the extreme contact point is at a given $r = R_b(t)$, which can be varied to predict cell body shape along spreading. B - Cell free edge between two plates is modelled by a constant mean curvature surface, symmetric around $z = 0$ and truncated by the plates at $z = \pm h/2$. C - Illustration of constant non-zero mean curvature (CMC) surfaces: (a) Sphere, (b) Cylinder, (c) Unduloid, and (d) Nodoid. D - Dorsal arc radius (R_{cap} on Fig. A) as a function of cell body contact radius R_b for the single plate geometry. Each color represent a single cell. Solid red line shows the result of simulations.

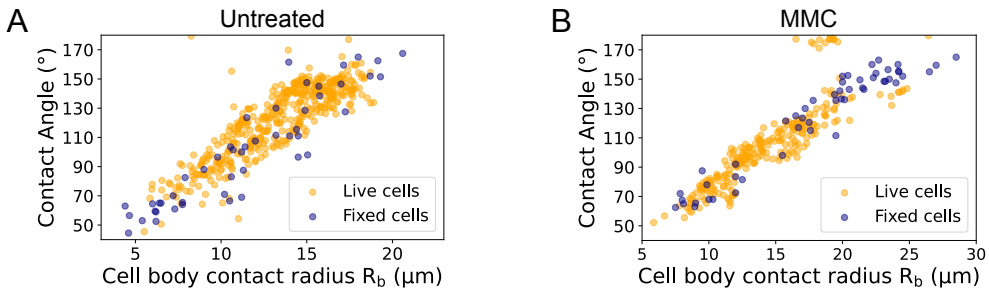

Fig.S 6. Comparison of three-dimensional cell shape in fixed (blue) and live (yellow) cells. A - Contact angle as a function of cell body contact radius for untreated cells. B - Contact angle as a function of cell body contact radius for mitomycin C-treated cells.

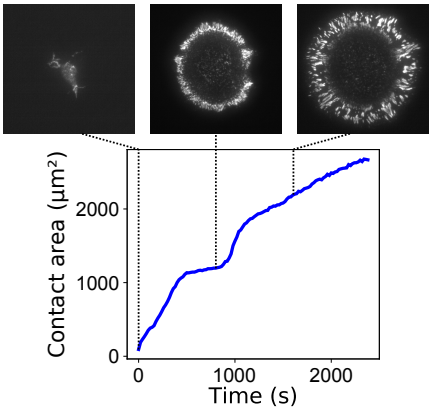

Fig.S 7. Rare event (n/N = 3/30) of cell spreading in two steps : spreading slow-down is followed by increase of spreading rate and second slow-down. Top row : TIRF imaging of paxillin-YFP along spreading. Left : Cell contact at t = 0s. Center : Cell contact at t=800s (first corona of paxillin clusters). Right : Cell contact at t=1600s (second corona of paxillin clusters). Bottom row : Cell contact area along spreading.

Supplementary movies legend

Movie 1. Time-lapse of Ref-52 fibroblast expressing paxilin-YFP spreading on a bi-dimensional glass substrate, imaged via TIRF microscopy. Time is in min:sec. Scale bar: 5µm.

Movie 2. Time-lapse of Ref-52 fibroblast expressing paxilin-YFP spreading between two parallel glass plate. Bottom cell-substrate contact is imaged via TIRF microscopy. Time is in min:sec. Scale bar: 5µm.

Movie 3. Time-lapse of Ref-52 fibroblast expressing paxilin-YFP treated with mitomycin C spreading on a bi-dimensional glass substrate, imaged via TIRF microscopy. Time is in min:sec. Scale bar: 5µm.

Movie 4. Time-lapse of Ref-52 fibroblast expressing paxilin-YFP treated with Y27632 at 8µM spreading on a bi-dimensional glass substrate, imaged via TIRF microscopy. Time is in min:sec. Scale bar: 5µm.

Movie 5. Time-lapse of Ref-52 fibroblast spreading on a glass plate seen in profile, imaged via bright-field microscopy. Time is in min:sec. Scale bar: 5µm.

Movie 6. Time-lapse of Ref-52 fibroblast spreading between parallel glass plate seen in profile, imaged via bright-field microscopy. Time is in min:sec. Scale bar: 5µm.

Movie 7. Segmentation and markers of cell profile along spreading of a Ref-52 fibroblast spreading on a glass plate. Scale bar: 5µm.

Movie 8. Shape changes and markers of the profile of a spherical cap of constant volume, mimicking cell spreading on a bi-dimensional substrate.

Movie 9. Shape changes and markers of the profile of a constant mean curvature surface in contact with two parallel planes, mimicking cell spreading between parallel plates.

Movie 10. Three-dimensional representation of shape changes of a constant mean curvature surface in contact with two parallel planes, mimicking cell spreading between parallel plates.

Movie 11. Time-lapse of Ref-52 fibroblast expressing paxilin-YFP spreading on a bi-dimensional glass substrate, imaged via TIRF microscopy, showing two steps of spreading and two successive focal adhesions ring forming. Time is in min:sec. Scale bar: 5µm.

Supporting references

1. J Étienne, et al., Cells as liquid motors: Mechanosensitivity emerges from collective dynamics of actomyosin cortex. *Proc Natl Acad Sci USA* **112**, 2740–2745 (2015).
2. E Moeendarbary, et al., The cytoplasm of living cells behaves as a poroelastic material. *Nat. Mater.* **12**, 253–261 (2013).
3. JL Maître, et al., Adhesion functions in cell sorting by mechanically coupling the cortices of adhering cells. *Science* **338**, 253–256 (2012).
4. PA Kralchevsky, K Nagayama, Capillary bridges and capillary-bridge forces in *Studies in Interface Science*. (Elsevier, Netherlands) Vol. 10, pp. 469–502 (2001).
5. H Nguyen, O Millet, G Gagneux, Exact calculation of axisymmetric capillary bridge properties between two unequal-sized spherical particles. *Math. Mech. Solids* **24**, 108128651878784 (2018).
6. AA Wahhod, Ph.D. thesis (Univ Grenoble Alpes) (2024) https://theses.fr/s297261.